Materials Today Bio 29 (2024) 101246

Contents lists available at ScienceDirect

Materials Today Bio

journal homepage: www.journals.elsevier.com/materials-today-bio

A bioengineered tumor matrix-based scaffold for the evaluation of melatonin efficacy on head and neck squamous cancer stem cells

Julia López de Andrés [a,b,c,d,1], César Rodríguez-Santana [b,e,f,g,1], Laura de Lara-Peña [a,b,c,d,1], Gema Jiménez [a,b,c,h], Germaine Escames [b,e,f,i,**], Juan Antonio Marchal [a,b,c,d,*]

[a] Biopathology and Regenerative Medicine Institute (IBIMER), Centre for Biomedical Research (CIBM), University of Granada, Granada, Spain
[b] Instituto de Investigación Biosanitaria ibs.GRANADA, University Hospitals of Granada, University of Granada, Granada, Spain
[c] BioFab i3D Lab-Biofabrication and 3D (Bio)printing Singular Laboratory, University of Granada, Granada, Spain
[d] Department of Human Anatomy and Embryology, Faculty of Medicine, University of Granada, Granada, Spain
[e] Instituto de Biotecnología, Centro de Investigación Biomédica, University of Granada, Granada, Spain
[f] Department of Physiology, Faculty of Medicine, University of Granada, Granada, Spain
[g] Department of Biomedicine, Aarhus University, Aarhus, Denmark
[h] Department of Health Sciences, University of Jaén, Jaen, Spain
[i] Centro de Investigación Biomédica en Red Fragilidad y Envejecimiento Saludable (CIBERFES), Instituto de Investigación Biosanitaria (Ibs), Granada, San Cecilio University Hospital, Granada, Spain

ARTICLE INFO

Keywords:
Head and neck squamous cell carcinoma
Cancer stem cells
Melatonin
Tumor microenvironment
Decellularized extracellular matrix
3D hydrogel
3D scaffold

ABSTRACT

Head and neck squamous cell carcinoma (HNSCC) presents a significant challenge worldwide due to its aggressiveness and high recurrence rates post-treatment, often linked to cancer stem cells (CSCs). Melatonin shows promise as a potent tumor suppressor; however, the effects of melatonin on CSCs remain unclear, and the development of models that closely resemble tumor heterogeneity could help to better understand the effects of this molecule. This study developed a tumor scaffold based on patient fibroblast-derived decellularized extracellular matrix that mimics the HNSCC microenvironment. Our study investigates the antitumoral effects of melatonin within this context. We validated its strong antiproliferative effect on HNSCC CSCs and the reduction of tumor invasion and migration markers, even in a strongly chemoprotective environment, as it is required to increase the minimum doses necessary to impact tumor viability compared to the non-scaffolded tumorspheres culture. Moreover, melatonin exhibited no cytotoxic effects on healthy cells co-cultured in the tumor hydrogel. This scaffold-based platform allows an *in vitro* study closer to HNSCC tumor reality, including CSCs, stromal component, and a biomimetic matrix, providing a new valuable research tool in precision oncology.

1. Introduction

Head and neck squamous cell carcinoma (HNSCC) ranks as the sixth most common solid cancer worldwide [1]. HNSCC is characterized for its aggressive behavior and high recurrence rates even after successful treatment [2]. While surgery, radiotherapy, and chemotherapy stand as effective modalities for treating early-stage tumors, their efficacy can be compromised by the emergence of resistance, rendering the outcomes of radiotherapy or chemotherapy unpredictable. The poor therapeutic response observed in patients with advanced HNSCC highlights the need for a deeper understanding of the mechanisms involved in the disease pathogenesis, as well as the search for novel treatments that can improve current therapeutic strategies or mitigating their side effects.

Recent studies have highlighted the oncostatic effects of melatonin (N-acetyl-5-methoxytryptamine, aMT) in different types of cancers [3]. Especially, in HNSCC strong evidence supports the efficacy of melatonin, both *in vitro* and *in vivo*, in regulating mitochondrial function and driving apoptosis by increasing mitochondrial reactive oxygen species (ROS) [4,5]. In this way, this indolamine reduces cell proliferation and enhances the effects of radio and chemotherapy [6,7].

* Corresponding author. Department of Human Anatomy and Embryology, Faculty of Medicine, University of Granada, E-18016, Granada, Spain.
** Corresponding author. Department of Physiology, Faculty of Medicine, University of Granada, E-18016, Granada, Spain.
E-mail addresses: gescames@ugr.es (G. Escames), jmarchal@ugr.es (J.A. Marchal).
[1] These authors contributed equally.

https://doi.org/10.1016/j.mtbio.2024.101246
Received 28 July 2024; Received in revised form 12 September 2024; Accepted 13 September 2024
Available online 14 September 2024

Current evidence demonstrates that tumor and pharmacological behavior largely depends on stromal components and their connection with malignant cells. The tumor microenvironment (TME) is a complex and dynamic network that continually changes its composition and state. It comprises diverse cell types such as fibroblast (FBs) and mesenchymal stem cells (MSCs), as well as extracellular matrix (ECM) molecules and signaling cues that can either inhibit or promote tumor growth [8]. Moreover, cancer stem cells (CSCs), which constitute a small subset within the tumor mass, have been identified as key orchestrators of the TME and tumor progression. In fact, CSCs are responsible for drug resistance and subsequent tumor recurrence in patients, rendering them a prime target of interest in cancer therapeutics [9].

Traditionally, cancer pharmacological studies have predominantly relied on conventional two-dimensions (2D) models. However, these models inadequately replicate the TME complexity, whether cell-cell or cell-matrix mimetic interactions, tumor vascularization, and many of the known features of tumors *in vivo*, contributing to the challenge of translating promising preclinical and basic research findings into clinical applications [10]. In contrast, three-dimensional (3D) models offer a more physiologically relevant platform, even incorporating patient-derived endogenous ECM proteins [11]. In this context, decellularized ECMs (dECMs) have emerged as a powerful biomaterial for mimicking the tumoral native context, as they preserve essential ECM components and provide mechanical integrity and biocompatibility of the native ECM [12]. In particular, given that tumor-associated FBs are the main producers of ECM biomolecules within the TME, FBs-derived dECM (*f*dECM) has been used to investigate the cellular behavior of tumor cell lines in several biofabricated 3D niches [13].

In the present study, we engineered a tumor matrix-based scaffold model of HNSCC microenvironment, integrating CSCs derived from the established HNSCC cell line Cal-27, along with representative stromal components including primary FBs and MSCs. For the non-cellular component, we developed and characterized a *f*dECM, which was incorporated with other biomaterials such as alginate and gelatin to fabricate a 3D hydrogel. This approach enabled the creation of a functional model that more accurately replicates the native conditions of HNSCC. Moreover, we investigated the antiproliferative effects of melatonin on this 3D model and evaluated its impact on the tumor phenotype. We compared these findings with outcomes observed in traditional non-scaffolded models. Through our study, we aimed to provide insights into the efficacy of melatonin in modulating HNSCC CSCs behavior within a physiologically relevant TME context.

2. Materials and methods

2.1. Cell cultures and treatment

2.1.1. Cell lines isolation and culture

The human HNSCC established cell line Cal-27 (ATCC: CRL2095) was obtained from the Cell Bank at the Scientific Instrumentation Centre of the University of Granada. MSCs and FBs were isolated from skin tissue from healthy subjects after aesthetic abdominal surgeries (ethics committee reference: 0467N-20) via enzymatic digestion with collagenase I (Sigma Aldrich). Cells were maintained in high glucose Dulbecco's Modified Eagle Medium (DMEM; Gibco), supplemented with 10 % fetal bovine serum (FBS; Gibco) and 1 % penicillin-streptomycin (Gibco) in culture flasks at 37 °C in a humidified atmosphere of 5 % CO2. FBs were used between passages 4 and 10. MSCs were used between passages 4 and 6.

2.1.2. Tumorspheres formation

For the enrichment of CSCs and the formation of primary spheres, Cal-27 tumor cells were washed with phosphate-buffered solution (PBS; Medicago) and resuspended at a concentration of 250,000 cells/well in ultra-low attachment 6-well plates (Corning) with serum-free culture medium composed of DMEM:F12 (Gibco), 1 % penicillin-streptomycin, 2 % B27 (Gibco), 10 μg/mL insulin-transferrin-selenium (ITS; Gibco), 1 μg/mL hydrocortisone (Sigma Aldrich), 4 ng/mL heparin (Sigma Aldrich), 10 ng/mL Epidermal growth factor (EGF; Sigma Aldrich), 10 ng/mL Fibroblast growth factor (FGF; Sigma Aldrich), 10 ng/mL Interleukin-6 (IL-6; Miltenyi Biotec) and 10 ng/mL Hepatocellular growth factor (HGF; Miltenyi Biotec). To obtain the secondary spheres, referred to as tumorspheres, cells from primary spheres were collected by centrifugation and dissociated with 0.25 % trypsin - 0.02 % EDTA (Gibco). Then, single cells were resuspended in the serum-free culture medium and plated at the same concentration of 250,000 cells/well in ultra-low adherence 6-well plates. After three days in low adherent culture with the described medium specific for CSCs enrichment [14], the cells were aggregated to form the secondary tumorspheres used in subsequent experiments.

2.1.3. CSCs characterization by flow cytometry

To characterize CSCs, flow cytometry studies were performed. Tumorospheres were trypsinized, washed and resuspended in PBS with 1 % bovine serum albumin (BSA; Sigma-Aldrich). Cells were centrifuged followed by the addition of fluorochrome-conjugated monoclonal antibodies for CD98 and CD44 (Miltenyi Biotec) according to the manufacturer's instructions and incubated at 4 °C in the dark for 12 min. After adding BSA, cells were centrifugated and resuspended in PBS and analyzed by flow cytometry in a FACSCanto II cytometer (BD Biosciences). ALDH1 activity was analyzed following the ALDEFLUOR kit-manufacturing instructions (Stem Cell Technologies), using harvested Cal-27 cell monolayer as a control.

2.1.4. Melatonin treatment

Melatonin (Fagron Ibérica S.A.U., Zaragoza, Spain) stock solution was prepared in 15 % propylene glycol (VWR)-PBS and filter-sterilized through a 0.2 μm pore filter (Labox). Melatonin treatment was refreshed at 24 h, and its effect was evaluated at 24 and 96 h after administration [15]. Tumorspheres cultured in suspension were treated with melatonin at concentrations of 500, 1,000, 1,500, 2,000 and 3,000 μM, while tumorspheres in hydrogels were treated with melatonin at concentrations of 2,000, 4,000 and 8,000 μM. Vehicle was added to the control groups.

2.1.5. Melatonin determination by HPLC

The determination of melatonin was measured from samples of the medium. The samples were then analyzed by HPLC (Shimadzu Europe GmbH, Duisburg, Germany) using a Waters Sunfire C18 column (150 × 4.5 mm, 5 μm). Melatonin fluorescence was measured using a Shimadzu RF-10A XL fluorescence detector (Shimadzu Europe GmbH) with 285-nm excitation and 345-nm emission wavelengths [16].

2.2. fdECM production

To enhance *f*ECM deposition, FBs were cultured in 150 × 20 mm petri dishes (Nunc). Once FBs reached full confluence, 0.17 mM L-ascorbic acid (Sigma Aldrich) and 0.34 mM L-proline (Sigma Aldrich) were added to the culture medium (described in section 2.1). The medium was refreshed every 2–3 days during 21 days.

After that period, the *f*ECM was washed with PBS and decellularized using different buffers. First, the *f*ECM was incubated in a chemical buffer containing 0.25 % triton X-100 (Sigma Aldrich) and 10 mM ammonium hydroxide (Sigma Aldrich) at 37 °C overnight (15 mL/petri dish). After washing it with PBS, the *f*ECM was collected in a tube using a scrapper and incubated in an enzymatic buffer of 0.25 % trypsin - 0.02 % EDTA at 37 °C for 30 min (2 mL/500 μL ECM). Finally, the *f*ECM was washed twice with PBS and centrifugated at 1,800 rpm for 10 min and incubated in an enzymatic buffer consisting on 10 mM TrisHCl (Sigma Aldrich), 50 U/mL DNase I (Sigma Aldrich) and 50 μg/mL RNase (Sigma Aldrich) at 4 °C overnight (2 mL/500 μL ECM). The resulting *f*dECM was washed with PBS and stored at 4 °C. After lyophilization, *f*dECM was

stored at −20 °C.

2.3. fdECM characterization

2.3.1. Quantification of collagens, glycosaminoglycans (GAGs) and DNA

Collagens content was measured using a colorimetric assay based on Sirius Red dye. First, matrices were incubated in Sirius Red dye (Sigma Aldrich) at a ratio of 1 mL per mg of matrix under agitation at room temperature for 1 h. The mixture was then centrifuged at 13,000 rpm for 15 min and the supernatant was removed. Then, 250 μL of alkaline reagent 0.1 M NaOH were added to the pellet and mixed thoroughly. Finally, 100 μL of the supernatant were taken to measure absorbance at 540 nm in a spectrophotometer. Collagen concentrations were calculated from a standard curve prepared with increasing concentrations of rat tail type I collagen (Sigma Aldrich).

GAG content was determined by a colorimetric method based on the dimethylmethylene blue (DMMB) assay. Matrices were incubated in a papain buffer (125 mg/mL papain in 0.1 M sodium phosphate with 5 mM EDTA and 5 mM cysteine-HCL, with a 6.5 pH) at a ratio of 1 mL per mg of matrix and incubated at 60 °C overnight. Then, 20 μL of the mixture were taken and mixed with 200 μL of DMMB, and the resulting solution was used to measure the absorbance at 570 nm in the spectrophotometer. GAG concentrations were calculated from a standard curve prepared with increasing concentrations of chondroitin sulfate (Sigma Aldrich).

DNA content was quantified using a fluorimetric assay based on DAPI. Samples were incubated in papain buffer as described above. Then, 50 μL of the mixture were taken and mixed with 50 μL of DAPI and incubated for 15 min. Fluorescence was measured with excitation and emission wavelengths of 340/360 nm and 440/460 nm, respectively, using a fluorescence microplate reader. DNA concentrations were calculated from a standard curve prepared with increasing concentrations of calf thymus DNA (Sigma Aldrich).

2.3.2. Histology

The matrices were fixed in 4 % paraformaldehyde (PFA; Sigma Aldrich) at room temperature for 20 min and embedded in paraffin. Masson's Thrichrome (MT), Van Gieson thricrome (VGT), Sirius Red (SR) and Toluidine Blue (TB) histological stains (Sigma Aldrich) were performed on 4 μm sections following the manufacturer's instructions. MT and VGT were used to contrast collagen fibers from cell nuclei, and other extracellular matrix structures. SR is used to analyze collagen, and TB, due to its high affinity for acidic tissue components, allows differentiation of nuclei and GAGs in histological sections. Images of the stained sections were obtained with a Leica DM 5500B microscope.

2.3.3. Immunofluorescence

The matrices were fixed in 4 % PFA (Sigma Aldrich) at room temperature during 20 min and embedded in Tissue Freezing Medium (Leica Biosystems). 8 μm sections were incubated in blocking buffer with 3 % BSA for 1 h at room temperature. Primary antibodies - Anti-Collagen I (ab254113, Abcam), anti-Collagen III (ab237238, Abcam), anti-Collagen IV (ab6586, Abcam), anti-Fibronectin (ab2413, Abcam) and anti-Laminin (ab11575, Abcam) - were used at a concentration of 1:300 and incubated at 4 °C overnight. The samples were then washed twice with PBS and incubated with goat anti-Rabbit IgG H&L Alexa Fluor® 488 (ab150077; Abcam) conjugated secondary antibody in a 1:500 concentration during 2 h at room temperature. Finally, after two washes with PBS, mounting medium with DAPI (Sigma Aldrich) was added and samples were imaged by Leica DM 5500 B microscope and processed using Image J Software (v.2.13.1).

2.3.4. Growth factors array

The retention of different human growth factors was assessed using the Human Growth Factor Antibody Array - Membrane (ab134002, Abcam), according to manufacturer's recommendations. Briefly, *f*dECM was treated with lysis buffer in a 1:1 ratio and, after centrifugation, supernatant was resuspended in blocking buffer in a 1:5 ratio. The membrane array was incubated in blocking buffer solution for 30 min. The sample was then added to the membrane and incubated at 4 °C overnight. Following multiple washes, the membrane array was incubated with 1 mL of biotin solution at 4 °C overnight and washed again. The membrane array was subsequently incubated with 1 mL of streptavidin solution for 3 h at room temperature. Finally, detection buffer solution was added and membrane arrays were visualized using ChemiDoc MP Imaging System (BioRad).

2.4. Cell-laden hydrogel biofabrication

Alginate solution (7,5 % w/v) was prepared by dissolving alginate brown algae powder (Sigma) in PBS. Gelatin solution (15 % w/v) was prepared by dissolving gelatin from porcine skin powder (Sigma) in PBS. Lyophilized *f*dECM was solubilized at 3 % in 1 mg/mL pepsin-0.1 M HCL and adjusted to physiological pH and salinity using 1M NaOH and PBS. For scaffold biofabrication, these three components were mixed in equal proportions and then combined with cellular pellets.

To incorporate into the hydrogel, Cal-27 tumorspheres were harvested and centrifuged. Additionally, for hydrogels containing the stroma-like component, MSCs and FBs in culture flasks were harvested using 0.25 % trypsin - 0.02 % EDTA (Gibco), centrifuged, stained with CellTracker Deep Red Dye (Invitrogen) following the manufacturer's instructions, and washed twice with PBS. After pelleting the cells, a careful mixture of tumorspheres (1×10^6 cells/mL) and/or stromal MSCs and FBs (5×10^5 cells/mL) with the hydrogel components was performed.

Hydrogel gelation occurred in two phases. Initially, gelatin was gelled at room temperature to provide the hydrogel with a specific shape, followed by incubation with 102 mM $CaCl_2$ at 37 °C for 20 min to cross-link the collagen and alginate. Finally, excess of $CaCl_2$ was removed, and serum-free tumorsphere medium (described in section 2.1.1) was added. Hydrogels were cultured in plates at 37 °C in a humidified atmosphere containing 5 % CO_2.

2.5. Cell viability assay

Viability assays were conducted using the fluorescent LIVE/DEAD™ Viability/Cytotoxicity Kit (Invitrogen) following the manufacturer's instructions. Briefly, hydrogels were washed three times with PBS, immersed in a solution of calcein AM (0.5 μL/mL) and ethidium homodimer-1 (2 μL/mL) in PBS, and then incubated at 37 °C for 30 min. Subsequently, hydrogels were washed three times with PBS and ezamined using a ZEISS LSM 900 FastAiry Scan 2 confocal microscope. Images were analyzed using Image J Software (v.2.13.1).

2.6. Cell proliferation assays

For CSCs tumorspheres, proliferation was assessed using the Cell Counting Kit 8 (CCK-8, Sigma Aldrich) following the manufacturer's protocol. Briefly, tumorspheres were treated with CCK-8 solution (10 μL/100 μL) and incubated for 1 h at 37 °C. Absorbance was then measured at 450 nm using a spectrophotometer. The size and morphology of tumorspheres were evaluated using the BioTek Lionheart LX Automated Microscope (Agilent).

In hydrogels, cell proliferation was measured using the alamarBlue™ HS Cell Viability Reagent (ThermoFisher Scientific) according to the manufacturer's instructions. Briefly, hydrogels were incubated with alamarBlue™ solution (10 μL/100 μL) during 1 h at 37 °C. Fluorescence was measured at excitation and emission wavelengths of 530 and 590 nm, respectively, using a fluorescence microplate reader.

2.7. Hydrogel immunofluorescence

The hydrogels were fixed in 4 % PFA at room temperature for 20 min and embedded in Tissue Freezing Medium. 4 μm sections were washed with Inmunofluorescence Buffer (IF), which consisted of a solution containing of 0.2 % Triton X-100 (Sigma Adrich) and 0.05 % Tween (Sigma Aldrich) in PBS. Subsequently, the sections were incubated in blocking buffer solution containing 1 % BSA (Sigma Aldrich) in IF

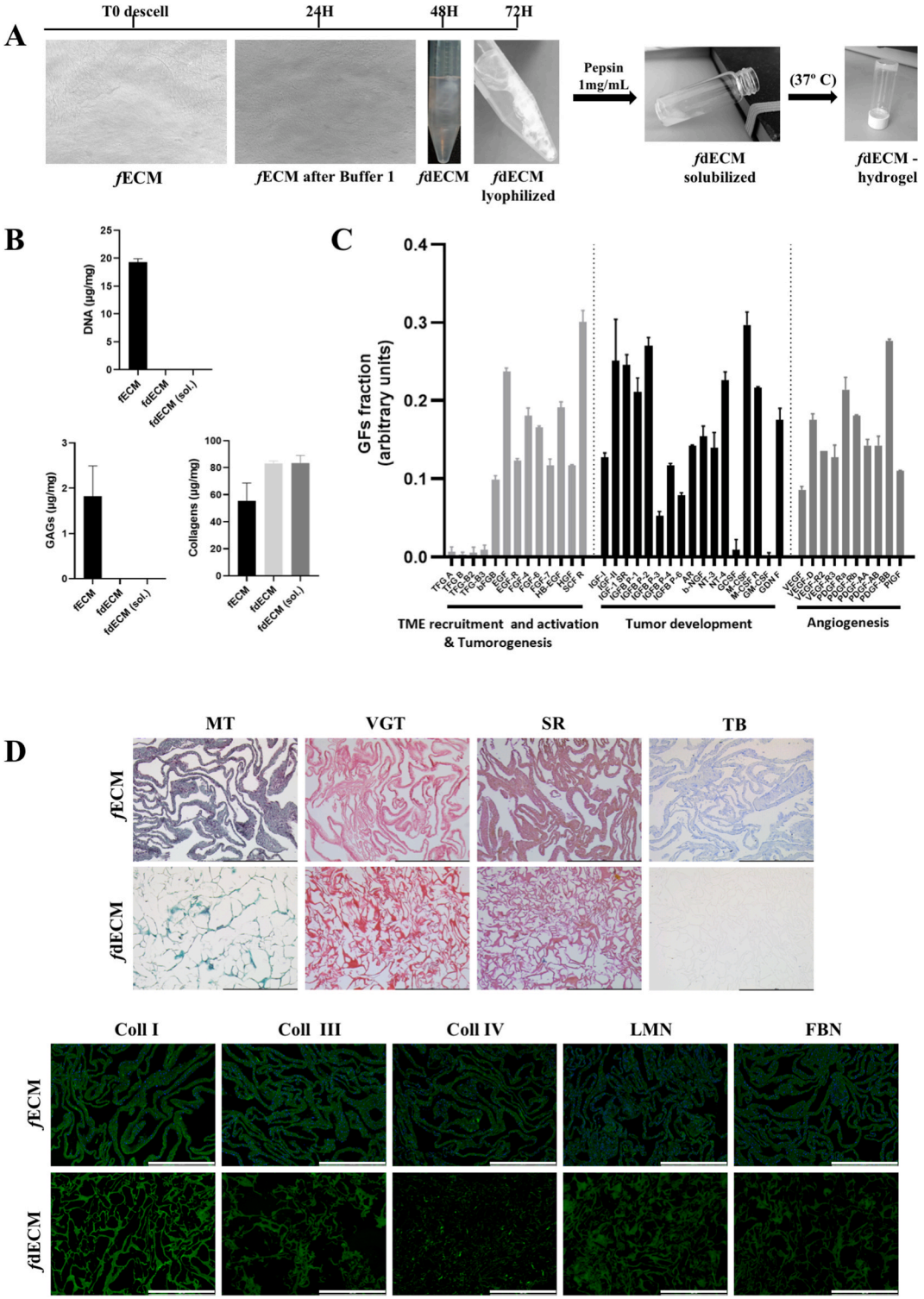

Fig. 1. fdECM characterization. (A) Process of deposition and collection of fdECM, and its macroscopic appearance after the different decellularization, solubilization and matrix gelation treatments. (B) Quantification of residual DNA, GAGs and collagens present in the matrices obtained (fECM), after the decellularization (fdECM) and solubilization (fdECM solub.) processes. (C) Quantification of the retained GF fraction of fdECM. (D) Representative images of histological staining of fECMs and fdECMs for Masson's Trichrome (MT), Van Gieson's Trichrome (VGT), Sirius red (SR) and Toluidine Blue (TB), and immunofluorescence of collagens type I (Coll I), III (Coll III) and IV (Coll IV), fibronectin (FBN) and laminin (LMN). Scale bar: 500 μm. (For interpretation of the references to color in this figure legend, the reader is referred to the Web version of this article.)

Buffer, for 40 min at room temperature.

Primary antibodies including anti-αSMA (ab5694, Abcam), anti-E-Cadherin (15148, Abcam), anti-N-Cadherin (ab18203, Abcam), anti-Vimentin (sc-6260, Santa Cruz), anti-CD133 (19898, Abcam) and anti-CD44 (ab243894, Abcam) were used at a 1:200 concentration and incubated at 4 °C overnight. Following incubation, the samples were washed twice with PBS and incubated with goat anti-Rabbit IgG H&L Alexa Fluor® 488 (ab150077; Abcam) and goat anti-Mouse IgG H&L Alexa Fluor® 594 (ab150116, Abcam) conjugated secondary antibodies at a 1:500 concentration for 2 h at room temperature. After two additional washes with PBS, mounting medium with DAPI (Sigma Aldrich) was applied, and the samples were imaged using a ZEISS LSM 900 FastAiry Scan 2 confocal microscope. Image processing was performed using Image J Software (v.2.13.1).

2.8. Quantitative RT-PCR

Total messenger RNA (mRNA) from tumorspheres within hydrogel was isolated using the RNeasy Fibrous Tissue Mini Kit (Qiagen) and reverse-transcribed into cDNA using the Reverse Transcription System kit (Promega). Quantitative PCR (qPCR) was conducted using a SYBR Green master mix (Promega) according to the manufacturer's recommendations. Gene expression levels for NANOG, OCT4, SOX2, SLUG, TWIST and VIMENTIN were normalized to those of the housekeeping gene glyceraldehyde 3-phosphate dehydrogenase (GADPH) and presented as fold change relative to the value of the control sample (Vehicle-Day 1). All the samples were assayed in triplicate for each gene. Genes primers were purchased from Sigma Aldrich (GAPDH, F 5′-TCGGAGTCAACGGATTTG and R 5′-CAACAATATCCACTTTACCAGAG; NANOG, F 5′-CTCCAACATCCTGAACCTCAGC and R 5′-CGTCACACCATTGCTATTCTTCG; OCT4, F 5′-CCTGAAGCAGAAGAGGATCACC and R 5′-AAAGCGGCAGATGGTCGTTTGG; SOX2, F 5′-GCTACAGCATGATGCAGGACCA and R 5′-TCTGCGAGCTGGTCATGGAGTT; SLUG, F 5′- ATCTGCGGCAAGGCGTTTTCCA and R 5′-GAGCCCTCAGATTTGACCTGTC; TWIST, F 5′-GCCAGGTACATCGACTTCCTCT and R 5′-TCCATCCTCCAGACCGAGAAGG; VIM, F 5′-AGGCAAAGCAGGAGTCCACTGA, and R 5′-ATCTGGCGTTCCAGGGACTCAT).

2.9. Statistical analysis

Statistical analyses were conducted using GraphPad Prism v. 8.0.1 software (GraphPad Software Inc., La Jolla, CA, USA). Data were expressed as mean ± standard error of the mean (S.E.M) form at least three independent experiments. Differences between experimental groups and their respective untreated controls were analyzed using unpaired Student's t-tests. A p-value <0.05 was considered statistically significant.

3. Results

3.1. fdECM generation and characterization

To obtain the *f*ECM, FBs were isolated from patient samples, and when they reached full confluence, the cells were treated with ascorbic acid and proline to enhance matrix deposition [17,18]. Following three weeks of treatment, the matrices underwent an optimal decellularization process (Fig. 1A) consisting in an efficient removal of DNA residues and nuclear debris from the cells while preserving ECM components to the maximum extent (Fig. 1B).

To prepare the matrix as the basis for a tumor hydrogel, the *f*dECM was solubilized with a pepsin solution (1 mg/mL), and subsequently analyzed for its ability to reticulate collagen fibers under physiological conditions of pH, temperature and salinity, and provide a gel solution. The gelling ability of the solubilized *f*dECM was proven by observing its maintenance as a hydrogel at the base of the vial when inverted (Fig. 1A).

For the characterization of the *f*dECM, the main macromolecules of the tumor ECM were analyzed, as well as the efficiency of the matrix decellularization process. For this purpose, DNA, GAGs and collagen remnants of the matrix were quantified before (*f*ECM) and after decellularization (*f*dECM), and after solubilization with pepsin (*f*dECM sol.) (Fig. 1B). The results indicate a complete decellularization of the matrix, and a high retention of collagens, the major component of the reconstituted matrices, but a drastic reduction of GAGs after application of the different decellularization buffers.

The tumor ECM serves not only as a scaffold for TME cells but also as a reservoir for growth factors (GF) crucial in tumor progression. Analysis of the GF array in the *f*dECM, revealed a retention of GFs involved in different tumor hallmarks, such as angiogenesis (vascular endothelial growth factor [VEGF], platelet-derived growth factor [PDGF]), activation of the TME (epidermal growth factor [EGF], fibroblast growth factor [FGF]), and inflammatory processes (Fig. 1C).

Histological staining of the *f*dECM (Fig. 1D) confirmed the quantification results, with predominant fibrillar collagen staining (MT, VGT, SR), absence of nuclei (MT, TB), and minimal staining for GAGs (TB). In addition, to assess the presence of active compounds, the matrices were characterized by immunofluorescence for specific markers including fibrillar proteins (collagen I and III), cell-matrix binding proteins (fibronectin), and basal lamina components (laminin and collagen IV). Positive expression of all markers was observed, along with the absence of nuclear debris (Fig. 1D).

Taken the results together, the generated *f*dECMs successfully recapitulate not only the structural component but also other bioactive components of tumor ECMs, thereby enhancing the fidelity of the generated models to the native tumor context.

3.2. Generation of HNSCC microenvironment model

To generate the HNSCC matrix-based scaffold tumor model, *f*dECM was formulated in combination with embedded cells that replicate the TME cellular component (Fig. 2A). To recreate the extracellular component, *f*dECM was blended with alginate and gelatin, to provide increased stiffness and structural robustness to the tumor hydrogels.

For the cellular component, CSCs enriched tumorspheres derived from the HNSCC Cal-27 line were used, given their pivotal role in drug resistance and tumor relapse due to their stemness properties. Moreover, for the TME simulation, the tumorspheres were co-embedded with primary MSCs and FBs, as the role of the stromal component in tumor progression is well-established. Indeed, the chemoprotective role of stromal cells in TME makes essential their presence in tumor models aimed at exploring the oncostatic effects of novel antitumor compounds.

First, the tumorspheres were characterized for the enrichment of CSCs using the previously described spheres culture medium [14]. The significant increment of the activity of aldehyde dehydrogenase 1 (ALDH1) enzyme was employed to assess CSC enrichment from a cell suspension of the Cal-27 tumor cell line [14] (Fig. 2A). Additionally, positive expression of the HNSCC stem cells membrane markers CD98 and CD44 [19–21] was evaluated in the tumorspheres. The analysis revealed a that all CSC markers were expressed over 96 % of the population.

To examine the potential cytotoxic effects of the hydrogel on the cells within the model, the tumorspheres, the stroma (comprising FBs and MSCs) and the combination of tumorspheres and stroma (referred to as TME) were cultured in the *f*dECM-based scaffolds. Cell viability was analyzed using the Live/Dead kit, and metabolic rate was measured using AlamarBlue®. The results revealed high cell viability (Fig. 2B) across all cell lines, both 24 h after seeding and after one week of culture. Live cells (stained green) predominated, with minimal presence of dead cells (nuclei marked in red). In addition, stromal cells exhibited a characteristic elongated morphology, indicating strong adherence to the substrate, in addition to the cytocompatibility of the hydrogel. Moreover, metabolic activity results (Fig. 2C) indicated cell proliferation in

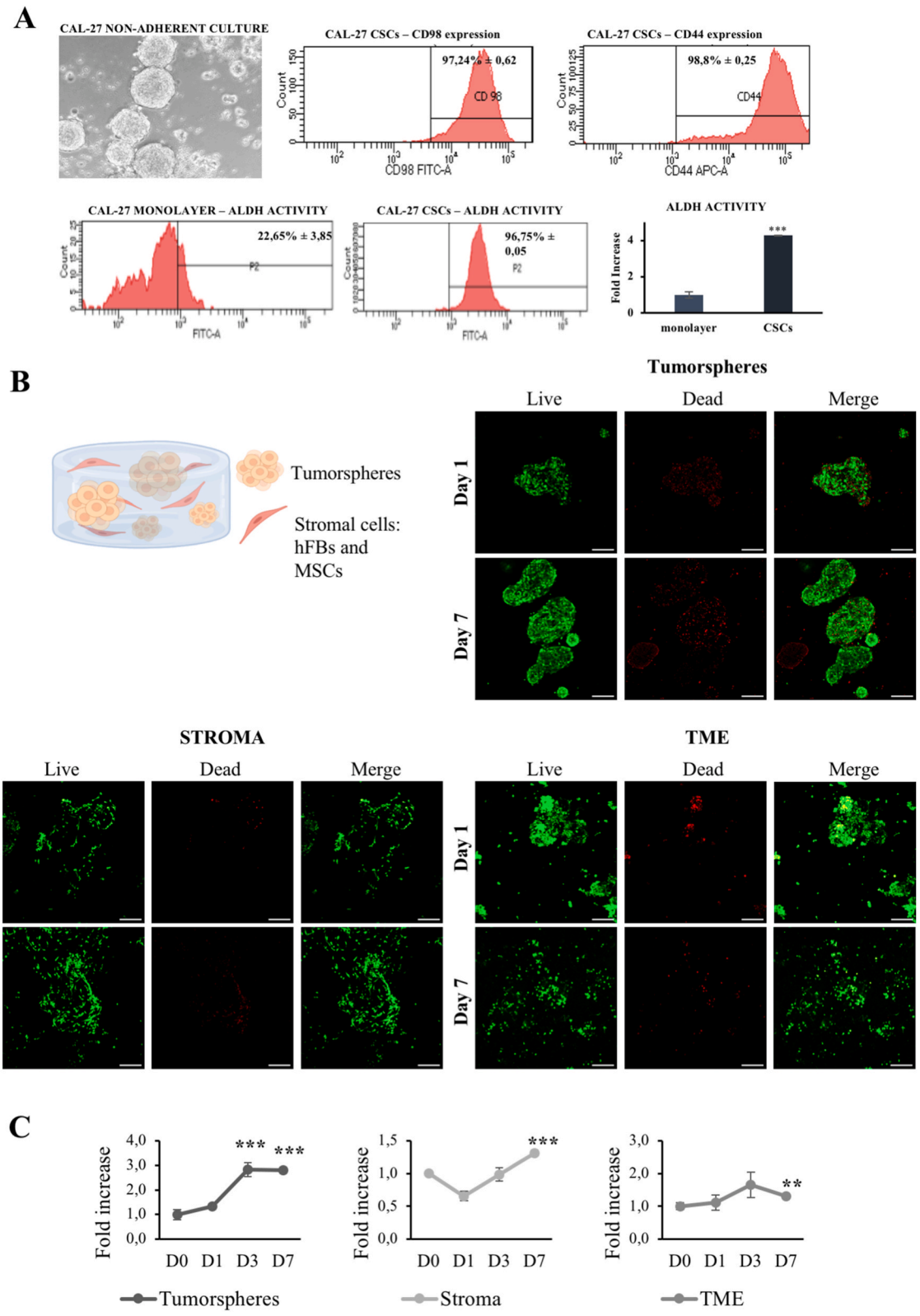

Fig. 2. HNSCC microenvironment model. (A) Characterization of Cal-27 CSCs. Image of tumorspheres grown in suspension with serum-free spheres medium (10×). Cytometry histograms of CD98 and CD44 CSCs cell-membrane markers expression. Percentage of ALDH1 activity of cells grown in monolayer or in suspension (cytometry histograms besides). (B) Schematic representation of the TME components embedded in the hydrogel. Confocal representative images of cell viability of tumorspheres, FBs and MSCs (stroma) and the co-culture of stroma and tumorspheres (TME) cultured in the hydrogel. Living cells shown in green and nuclei of death cells in red. Scale bar: 200 μm. (C) Proliferation assay of the tumorspheres, FBs and MSCs (stroma) and the co-culture of stroma and tumorspheres (TME) cultured in the hydrogel. (For interpretation of the references to color in this figure legend, the reader is referred to the Web version of this article.)

all models, with tumorspheres cultured alone exhibiting a notably higher proliferation rate (fold increase 2.79 ± 0.13 at day 7) compared to when cultured alongside the rest of the microenvironment (fold increase 1.32 ± 0.04 and 1.30 ± 0.06 for stroma and TME respectively at day 7).

3.3. Evaluation of the oncostatic effect of melatonin on HNSCC tumor cells

3.3.1. Antiproliferative effect of melatonin on HNSCC tumorspheres

To analyze the oncostatic effect of aMT on HNSCC tumorspheres, we followed the previously described treatment regime (Section 2.1.4.). The target effect was measured 24 h (day 1) and 96 h (day 4) after the last dosed pulse (Fig. 3). To ensure that aMT level remained consistent and, therefore, the dose available to the cells matched the intended treatment regimen, aMT concentration in the medium was monitored for 96 h following application, under the same culture conditions as the study models. Fig. 3A demonstrates the concentration remained stable without significant degradation of aMT over the maximum study time. This consistent pattern was maintained for all subsequent assays across different models.

Because CSCs offer increased drug resistance than their differentiated counterparts, a dose-response study was conducted at increasing doses of aMT, ranging from 500 μM to 3,000 μM (Fig. 3B), following 24 and 96 h of treatment. Results showed that melatonin significantly reduced cell viability in a dose-dependent manner at both time points of the assay. At day 1, the concentration that effectively eliminated approximately 50 % of the cell population was 1,500 μM (***$p < 0.001$). With prolongated exposure, by day 4, the concentration reducing approximately 50 % of the cell population decreased to 500 μM (***$p < 0.001$). In addition, in all cases there was a negative impact of the vehicle on the tumor cells, although considerably less pronounced than that induced by the drug ($^{###}p < 0.001$ and $^{##}p < 0.01$).

This effect was also visually perceived in the HNSCC tumorspheres (Fig. 3C), with a noticeable reduction in spheres size and increased disaggregation of tumor cells in the treated conditions compared to the

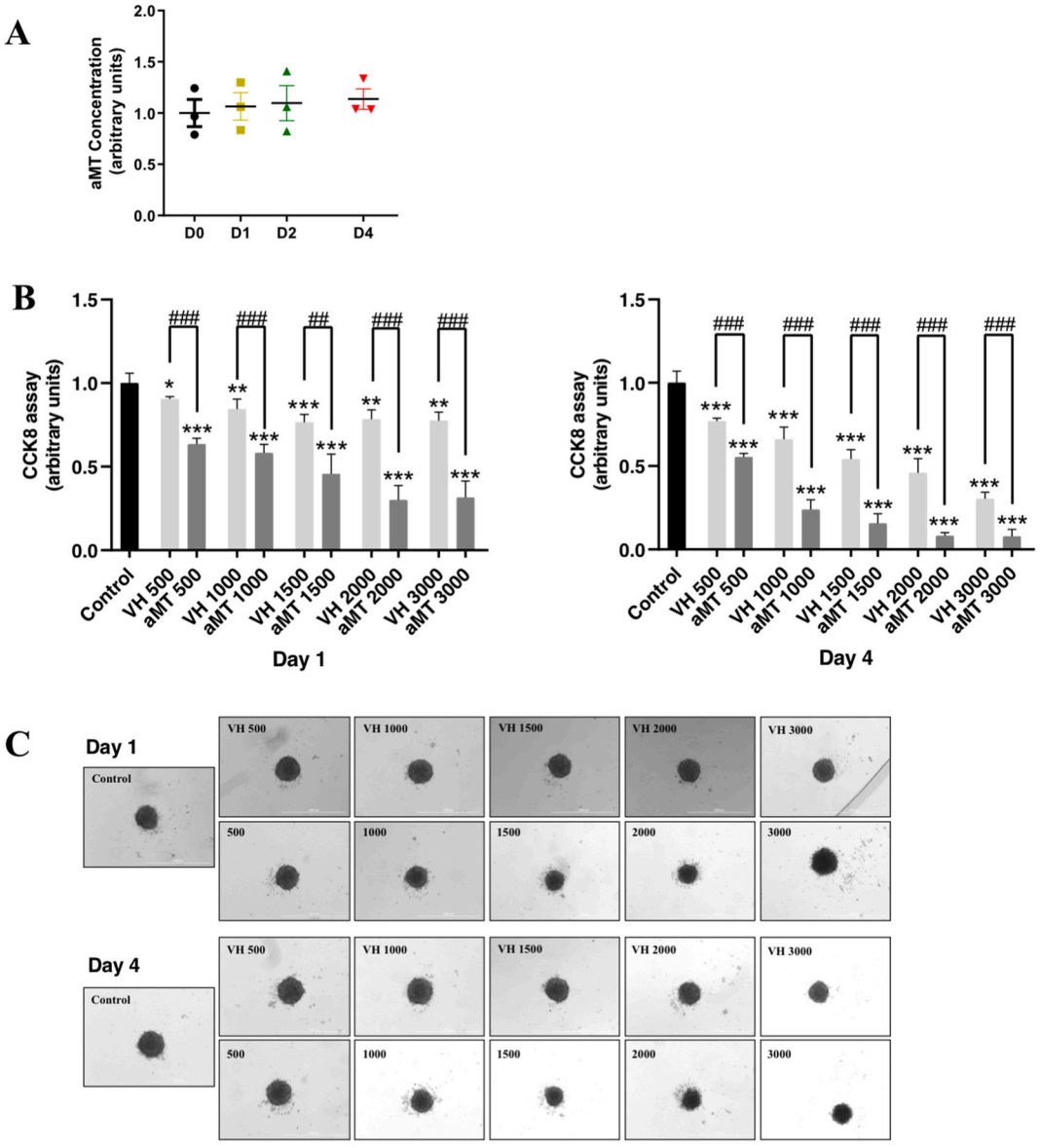

Fig. 3. ct in HNSCC tumorspheres. (A) Quantification of aMT concentration in the culture medium monitored over four days. (B) Cell cytotoxicity assay of the tumorspheres at increasing concentrations of aMT, compared to their corresponding vehicle control (VH), at day 1 and 4 after application of the last dose of aMT (C) Representative images of the aMT-treated tumorspheres and their corresponding vehicle controls. The aMT doses applied were: 500, 1,000, 1,500, 2,000 and 3,000 μM. Scale bar: 1000 μm.

control condition. This effect was especially pronounced at day 4, and from dose 1,500 and higher, where the size of the tumorspheres was drastically reduced, and its structure considerably altered.

3.3.2. *Antiproliferative effect of melatonin on HNSCC tumorspheres cultured in the hydrogel*

For the treatment of hydrogel-cultured tumorspheres, the same guideline was applied, but with increasing concentrations of aMT applied to the matrix-embedded models. Treatment began with doses that exceeded half of the damaged population observed in non-scaffold cultures: specifically, 2,000, 4,000, and 8,000 μM.

Through the dose-response assay, a dose-dependent effect of aMT on HNSCC CSCs was again noticeable (Fig. 4A). Interestingly, even though the decrease is statistically significant, none of the doses were sufficient to eliminate 50 % of the tumor population at day 1. By day 4, the 4,000 μM dose did have an inhibitory effect on half of the population (***$p < 0.001$). Beyond this concentration, an increase in aMT dose did not significantly enhance cell death, suggesting a potential saturation point for cellular assimilation of this compound.

Moreover, in the 3D models the effect of vehicle was clearly reduced, only significantly altering cell viability at 8,000 μM on day 1 (*$p < 0.05$), but totally innocuous for medium and low doses (Fig. 4 A). Notably, this result together with the significant difference in the minimum inhibitory doses between free or gel-cultured tumorspheres, 500 μM and 4,000 μM at day 4 respectively (Figs. 3B and 4A), underscores the strong protective effect exerted by ECM in tumor contexts, ratifying the importance it acquires in tumor progression and chemoresistance.

The antitumor efficacy of aMT was further evaluated by confocal microscopy using the cell viability assay (Fig. 4B). The dose of aMT 4,000 μM was chosen for subsequent assays, since it has an inhibitory effect on half of the population, and its vehicle dose does not alter the cell population. Remarkably, treated hydrogels at day 4 exhibited a significant increase in dead cells (red-labeled nucleus) and extensive cell disintegration compared to the initial day and untreated controls

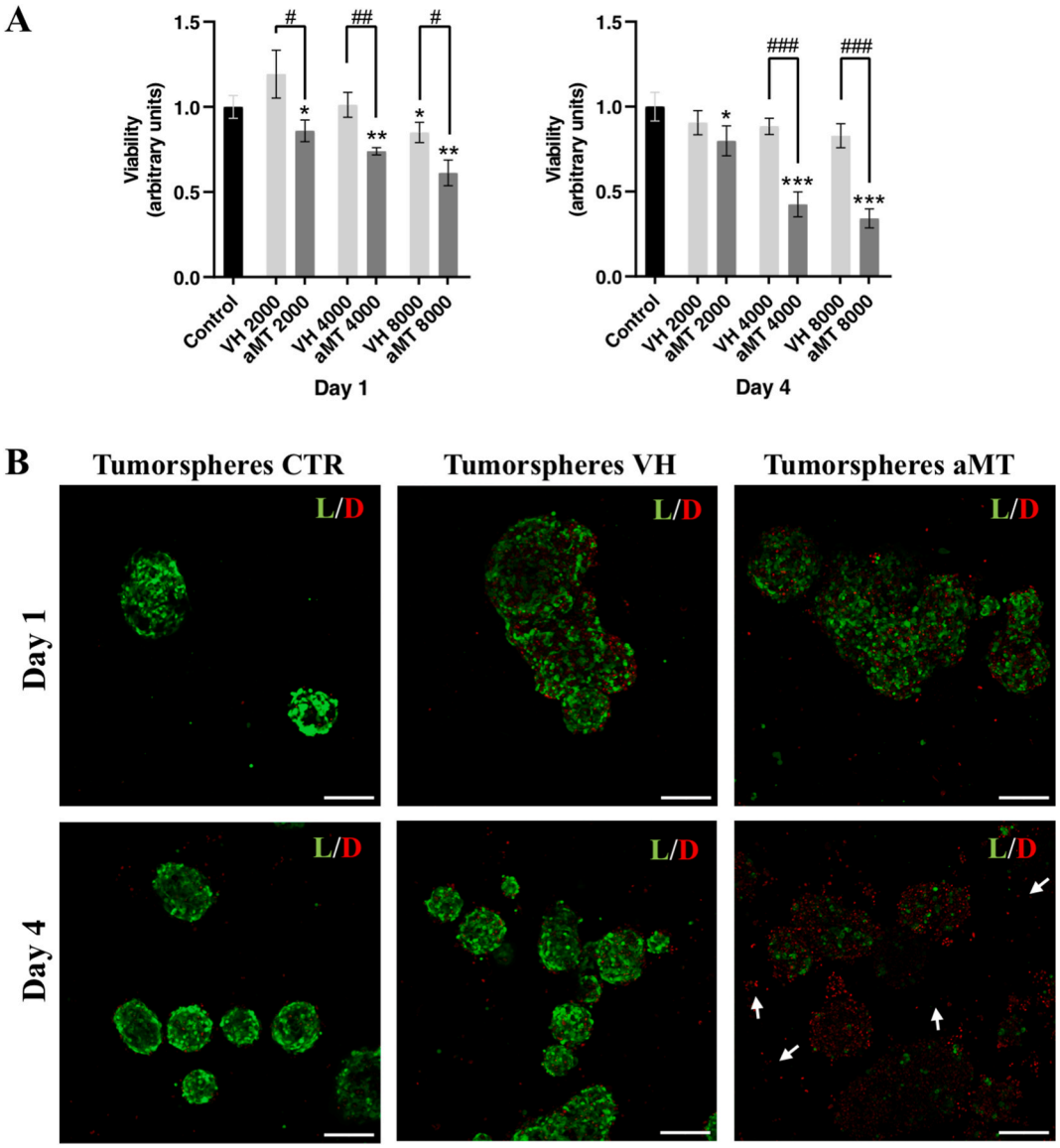

Fig. 4. aMT antiproliferative effect in HNSCC tumorspheres viability cultured in the tumor hydrogel. (A) Cell cytotoxicity assay of tumor spheres cultured in hydrogel at increasing concentrations of aMT, compared to their corresponding vehicle control, at day 1 and 4 after application of the last dose of aMT. (B) Representative confocal images of cell viability of tumorspheres cultured in hydrogel, untreated (CTR tumorspheres), administering vehicle alone (tumorspheres VH) and with aMT 4,000 μM (tumorspheres aMT), after 1 or 4 days of treatment. White arrows point to the isolated cells from tumorspheres disaggregation. Living cells shown in green and nuclei of death cells in red. Scale bar: 200 μm. (For interpretation of the references to color in this figure legend, the reader is referred to the Web version of this article.)

(Fig. 4B, white arrows), which showed compact spheres with predominantly green labeling of live cells.

To investigate the impact of melatonin on the properties of HNSCC CSCs, stemness and epithelial-mesenchymal transition (EMT) related markers were analyzed via qPCR and immunofluorescence. A notable disaggregation of tumorspheres was observed, consistent with previous findings, so stemness-related membrane marker CD44, visible 24 h after treatment, was no longer detectable at the endpoint, while CD133 persist in the individualized tumoral cells (Fig. 5A). However, qPCR analysis of NANOG, OCT4, and SOX2 gene expression revealed a significant increase in OCT4 and SOX2 after treatment (**$p < 0.01$) (Fig. 5B), suggesting that the surviving cell population, and consequently the most resistant, may exhibit enhanced stemness phenotype. On the contrary, epithelial-mesenchymal transition (EMT) markers basal expression was observed by immunofluorescence of N-Cadherin, Vimentin, α-Smooth Muscle Actin (αSMA), and E-Cadherin (Fig. 5A) at

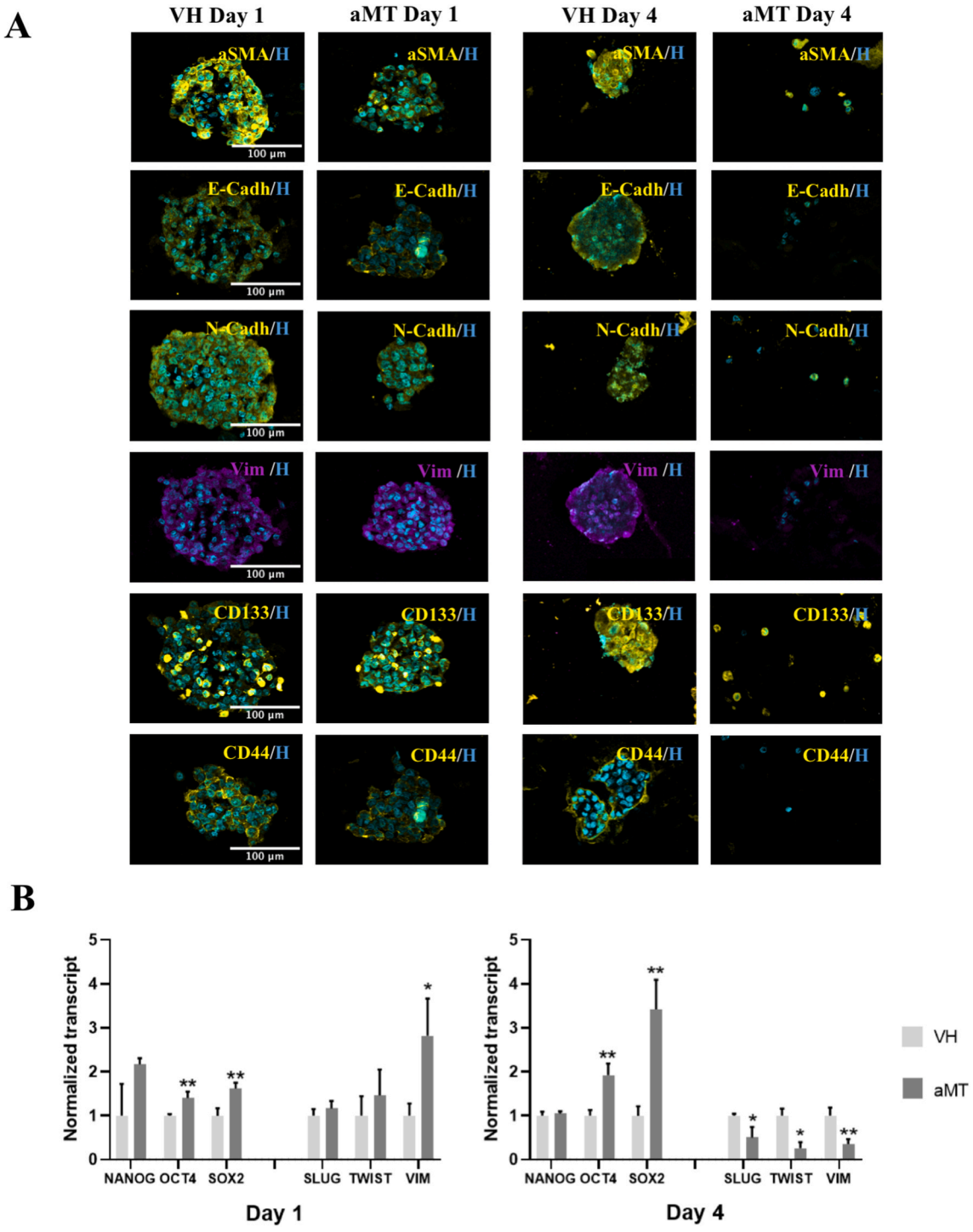

Fig. 5. aMT effect in HNSCC tumorspheres phenotype cultured in the tumor hydrogel. (A) Representative immunofluorescence images of CD44, CD133, αSMA, Vimentin, E-Cadherin, and N-Cadherin in the tumorspheres cultured in the hydrogel and treated with aMT 4,000 μM or vehicle, after 1 or 4 days of treatment. Scale bar: 100 μm. (B) qPCR expression analysis of NANOG, OCT4, SOX2, SLUG, TWIST, and VIMENTIN (VIM) genes in the tumor spheres cultured in the hydrogel and treated with aMT 4,000 μM or vehicle after 1 or 4 days of treatment. Normalized with endogenous GAPDH and relative to the day 1 control.

day 1, but not noticeable at day 4, as the tumorspheres conformation was disaggregated and cell markers visually reduced. Additionally, a significant decrease in expression of SLUG (*p < 0.05), TWIST (*p < 0.05), and VIMENTIN (**p < 0.01) was measured at day 4 by qPCR (Fig. 5B). The significant reduction in markers associated with tumor metastasis and invasion compared to the control suggests an effect of melatonin in the regulation of this tumor hallmark.

3.4. Antiproliferative effect of melatonin in HNSCC TME

Considering the previously described influence of TME on the pharmacodynamics of antitumor compounds, melatonin was also tested in the TME matrix-based scaffold models outlined in section 3.2, comprising complex cellular component, with tumorspheres and stroma, and the mimetic ECM (Figs. 6 and 7). A cell viability assay was conducted using the Live/Dead kit. To discern on which target aMT acted, stromal cells were previously labeled with a vital dye (CTDR, violet) to differentiate them from unlabeled tumor cells. The same regimen as previously described was applied, with a concentration of aMT set at 4,000 μM.

It was observed that stromal cells exhibited high viability in treated conditions after 24 and 96 h of drug exposure, maintaining their characteristic elongated spindle-shaped phenotype (Fig. 6). This data demonstrates the absence of cytotoxic effect of aMT on healthy cells, as well as no apparent alteration in their signature phenotype.

Additionally, the effect of aMT was assessed in the TME matrix-based scaffold model including the different cell subtypes. The stromal cells (FBs and MSCs) were previously marked with CTDR, enabling differentiation between the effects on cell viability in stromal cells (marked in magenta) and tumor cells (unmarked). Consequently, in the model, we observed a significant impact of aMT on tumor cells (unmarked), whereas stromal cells (magenta) co-stained with calcein, indicating robust viability (Fig. 7). The importance of this result relies on the possibility of co-culturing different TME cell lineages in a representative tumor model, and exploring simultaneously the different pharmacological effect on several tumor components, in order to obtain more relevant conclusions.

4. Discussion

The field of oncology research faces a significant challenge in translating pharmacological trials into clinical practice, with over 97 % of cancer drug candidates failing in clinical trials and never obtaining FDA approval [22]. One of the reasons identified is the lack of research platforms that faithfully represent the pathological processes of this disease, and the pharmacokinetics of the proposed products. While *in vivo* xenograft models represent a highly advanced model, which has provided valuable insights, they still have some limitations. As discussed by Bonartsev et al., it is challenging to monitor parameters such as cell growth, or the specific response to certain drugs, and they undergo a carcinogenic process that fails to fully mimic human physiology [23]. Engineered tumor models offer a complementary approach for more comprehensive *in vitro* investigation closer to clinical reality.

To generate 3D tumor models, it is essential to integrate both the biophysical properties of the tissues and materials that promote biomolecular interactions within the tumor niche. *In vitro* reconstituted matrices are a suitable candidate that meets these criteria by retaining structural and biochemical components of human tissues [12]. In this study, we designed a tumor matrix-based scaffold model using dECM obtained from patient-derived primary FBs. It has been postulated that cell culture-derived dECM minimizes batch-to-batch variability associated with using native tissues directly as an ECM source, making it a better candidate for chemoresistance studies and pharmacological screening [24]. Indeed, FBs-derived matrices have been successfully used for tumor models, aiding in the study of tumor progression and drug resistance [13,18,25,26], although many of them are derived from isolated mouse FBs and, therefore, may present key differences with those obtained from human tissues. Our generated matrix exhibited a high composition of fibrillar collagen and expressed key proteins for tumor development such as fibronectin, collagen IV or laminin, thus resembling the HNSCC microenvironment [8,27–29]. The decellularization process produced a soft hydrogel capable of cross-linking under physiological conditions. The *f*dECM also retained growth factors involved in angiogenesis, tumor growth, TME activation, and other tumor hallmarks, including VEGF, PDGF, EGF, or FGF [30–32], thereby providing functionality to the reconstituted matrix. Moreover, the tumoral ECM exerts a chemoprotective role, not only acting as a physical barrier against drugs, but also promoting the maintenance of a tumor phenotype with increased resistance to treatment [33–35]. Our *f*dECM retain a complete set of GFs that can drive tumor cell dedifferentiation and generate a stem niche, including interleukin 4 (IL-4), interleukin (IL-6), EGF, and HGF [35–38], thus with the potential to provide more accurate pharmacological responses. This *f*dECM was combined with alginate and gelatin to provide consistency and microstructure to the hydrogels. Similar combinations have proven effective in previous HNSCC models [39,40], although based on animal-derived tissue matrices.

In addition to evaluating the extracellular component, different TME cell lineages were co-cultured. CSCs are highly responsible for drug resistance and tumor relapse [41]. In the current work, CSCs were cultured as tumorspheres, as this spherical geometry closer mimics the *in vivo* scenario of solid tumors [42]. Tumorspheres were co-cultured with patient-derived stromal cells, including MSCs and FBs. Stromal lines are fundamental not only for the production of ECM, but also for the progression of HNSCC [43–45], the maintenance of the CSC population [46–50], or chemoresistance mechanisms [50–52]. Therefore, their incorporation in 3D models is essential to faithfully reconstruct the TME. Our bioengineered tumor matrix-based scaffold model promoted cell adhesion, viability and proliferation in a biomimetic approach, as well as the acquisition of the characteristic stromal spindle-shaped phenotype [53], supporting the development of the tumor niche.

The inhibitory effects of melatonin against numerous types of cancer are currently under extensive investigation. Specifically, robust evidence supports melatonin's oncostatic effects in HNSCC, both *in vitro* and *in vivo*, along with its potential as an adjuvant to other chemotherapeutics [5,15,54,55]. However, despite various clinical trials confirming the anticancer properties of melatonin, existing discrepancies underscore the necessity for more comprehensive studies [54]. One of the main reasons for this controversy is the limited understanding of the mechanisms underlying its anticancer effects, displaying a dual role in healthy and tumoral cells, which hampers its clinical application. This explains why melatonin has primarily gained importance as an adjuvant and protective agent in clinical settings [4,54,56]. On the other hand, melatonin has also been shown to target CSCs in various tumor type [57–60], leading to a decrease in stemness and EMT markers. Given these promising results, we investigated the oncostatic effect of melatonin on engineered HNSCC matrix-based scaffold models based on CSCs. Our findings demonstrated a strong antiproliferative effect of melatonin on CSCs tumorspheres both free and embedded in the reconstituted matrix. Interestingly, effective doses were higher in hydrogels than in tumorspheres cultured without supporting *f*dECM, in line with other trials using advanced HNSCC tumor models [39,42,61]. The protective effect of the matrix can be exerted through various mechanisms. On one hand, its structure and density act as a physical barrier that reduces drug availability in the tumor microenvironment [8]. In addition, matrix components, along with the growth factors and cytokines it retains, can modulate the resistance mechanisms of tumor cells [24]. Additionally, a decrease in EMT markers was observed, consistent with previous *in vitro* and animal model experiments [5]. Furthermore, some of these assays reported a decrease in stemness markers. In contrast, our work reveals an increase in stemness markers after treating the CSCs tumorspheres. This may not be contradictory, as

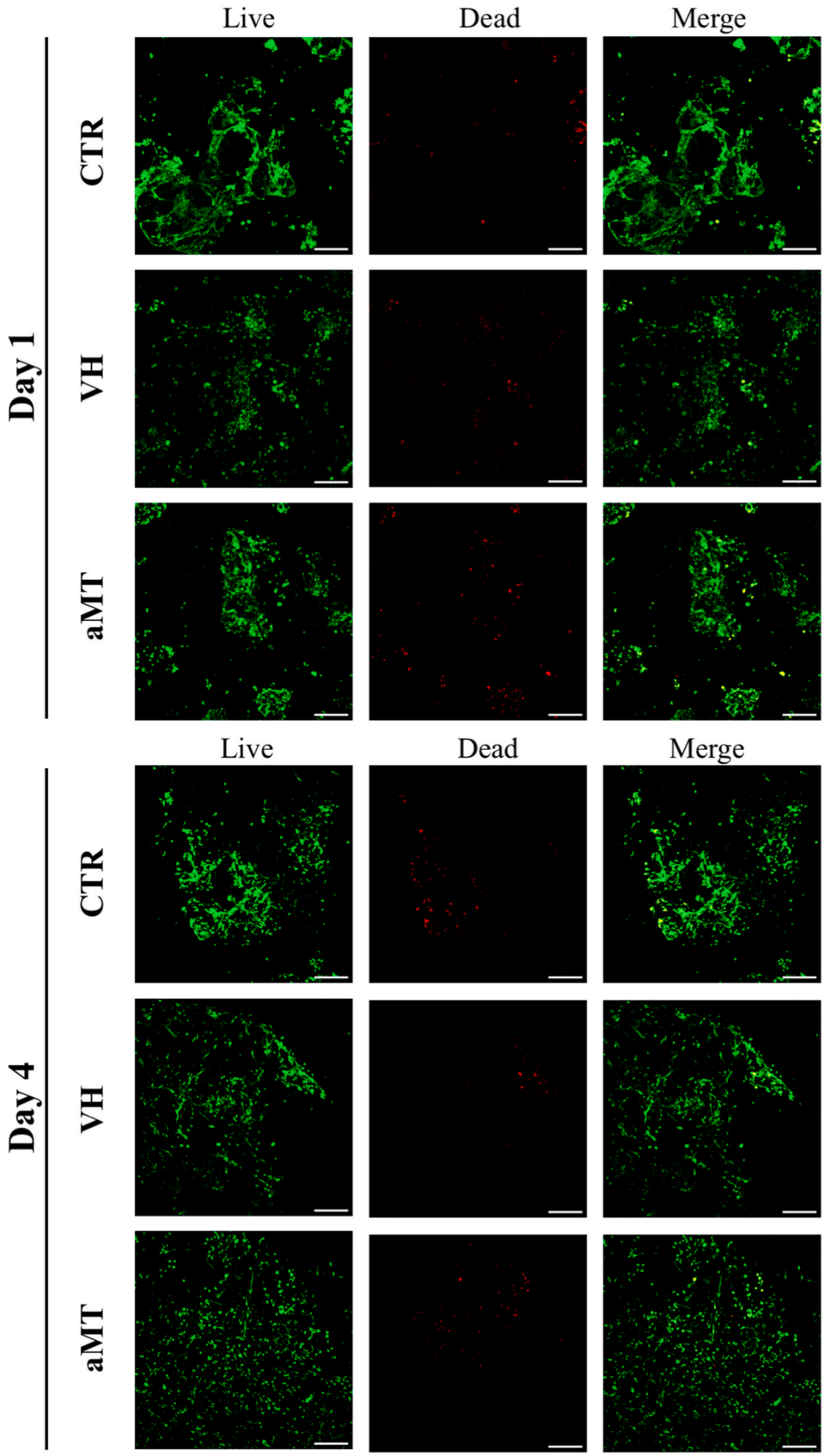

Fig. 6. aMT effect in HNSCC stromal cells viability cultured in the tumor hydrogel. Representative confocal images of cell viability of FBs and MSCs (stroma) cultured in hydrogel, untreated (CTR), administering vehicle alone (VH) and aMT 4,000 μM (aMT), after 1 (A) or 4 (B) days of treatment. Living cells shown in green and nuclei of death cells in red. Scale bar: 200 μm. (For interpretation of the references to color in this figure legend, the reader is referred to the Web version of this article.)

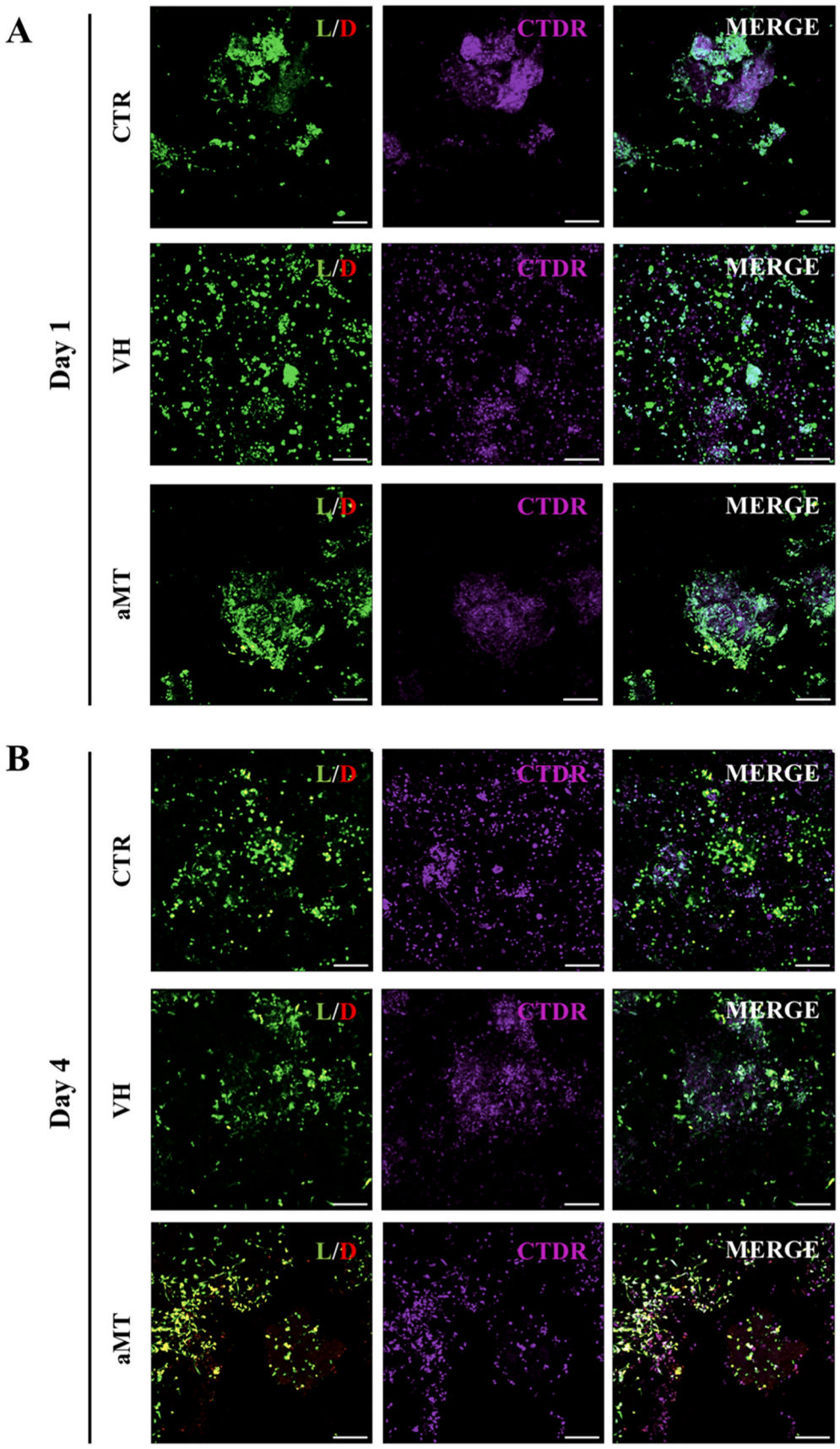

Fig. 7. aMT effect in HNSCC TME viability cultured in the tumor hydrogel. Representative confocal images of cell viability of HNSCC tumorspheres, FBs and MSCs (TME) cultured in hydrogel, untreated (CTR), administering vehicle alone (VH) and with aMT 4,000 μM (aMT), after 1 (A) or 4 (B) days of treatment. MSCs and FBs are stained with CTDR (violet). Living cells shown in green and nuclei of death cells in red. Scale bar: 200 μm. (For interpretation of the references to color in this figure legend, the reader is referred to the Web version of this article.)

those previous studies are based on a mixed population, comprised of cancer cells at different stages of differentiation, where CSCs represent a low population of the tumor bulk. Alternatively, our study prioritizes CSCs, given their established status as a high-priority therapeutic target in this tumor type, with melatonin specifically targeting this population [57–59]. We demonstrated that the surviving CSCs population presented an enhanced stem phenotype, thus deeper describing the phenotype of chemoresistant cells, and allowing for further therapeutic targeting. Since melatonin presented strong effects as an adjuvant to established therapies against HNSCC [62,63], its combinations with other drugs targeting CSCs could effectively prevent tumor relapse after treatment.

Finally, the effect of melatonin was tested in the complete tumor model, including the stromal component of TME, confirming the non-cytotoxic effect of melatonin in healthy stromal cells isolated from patients [64,65]. In fact, melatonin has been proved to clearly ameliorate the side effects of chemotherapy, therefore so highly valued in the clinical arena [66–68]. Due to the high tumor heterogeneity among patients, obtaining robust results on the effect of antitumor compounds is challenging. Personalized models that incorporate patient-derived *f*dECM and support the cultivation of patient-derived cells may represent a significant advance in oncology research [69]. The tumor matrix-based scaffold platform proposed in this work brings us closer to personalized medicine, enabling the incorporation of other members of the tumor niche, and simultaneous study of different therapeutic targets in a HNSCC neoplastic model.

5. Conclusion

The development of biomimetic models for HNSCC based on *f*dECM allows for a closer and more realistic study of the oncostatic effects of new anti-tumor treatments. Through these models, in this study the antiproliferative effect of melatonin on CSCs has been demonstrated, even in highly protective environments. Moreover, it has enabled the examination of melatonin's impact on invasion processes and the analysis of resistant cell phenotypes. The hydrogel also facilitates the inclusion of other components of the TME, thereby enabling the study of possible drug side effects. The potential adaptation of this model to patients, with the inclusion of endogenous ECM cells and proteins or immune cells, may lead to a more personalized medicine, tailoring treatment guidelines and improving outcomes for HNSCC patients.

CRediT authorship contribution statement

Julia López de Andrés: Writing – original draft, Methodology, Investigation, Formal analysis, Data curation, Conceptualization. **César Rodríguez-Santana:** Writing – original draft, Methodology, Investigation, Formal analysis, Data curation, Conceptualization. **Laura de Lara-Peña:** Writing – original draft, Methodology, Formal analysis, Data curation. **Gema Jiménez:** Writing – review & editing, Supervision, Investigation, Formal analysis. **Germaine Escames:** Writing – review & editing, Supervision, Resources, Funding acquisition, Conceptualization. **Juan Antonio Marchal:** Writing – review & editing, Visualization, Supervision, Resources, Project administration, Funding acquisition, Conceptualization.

Declaration of competing interest

The authors declare that they have no known competing financial interests or personal relationships that could have appeared to influence the work reported in this paper.

Data availability

Data will be made available on request.

Acknowledgments

This study was funded by grants from the Plan Propio of University of Granada (PPJIB2020.3), the MCIN/AEI/10.13039/501100011033/(PID2020-115112RB-I00), the European Union NextGenerationEU/PRTR (PID2022-140151OB-C22), and the Chair "Doctors Galera-Requena in cancer stem cell research" (CMC-CTS963).

References

[1] H. Sung, J. Ferlay, R.L. Siegel, M. Laversanne, I. Soerjomataram, A. Jemal, F. Bray, Global cancer statistics 2020: GLOBOCAN estimates of incidence and mortality worldwide for 36 cancers in 185 countries, CA A Cancer J. Clin. 71 (2021) 209–249, https://doi.org/10.3322/CAAC.21660.

[2] D.E. Johnson, B. Burtness, C.R. Leemans, V.W.Y. Lui, J.E. Bauman, J.R. Grandis, Head and neck squamous cell carcinoma, Nat. Rev. Dis. Prim. (6) (2020 61 2020) 1–22, https://doi.org/10.1038/s41572-020-00224-3.

[3] Y. Zhao, C. Wang, A. Goel, A combined treatment with melatonin and andrographis promotes autophagy and anticancer activity in colorectal cancer, Carcinogenesis 43 (2022) 217–230, https://doi.org/10.1093/CARCIN/BGAC008.

[4] J. Florido, L. Martinez-Ruiz, C. Rodriguez-Santana, A. López-Rodríguez, A. Hidalgo-Gutiérrez, C. Cottet-Rousselle, F. Lamarche, U. Schlattner, A. Guerra-Librero, P. Aranda-Martínez, D. Acuña-Castroviejo, L.C. López, G. Escames, Melatonin drives apoptosis in head and neck cancer by increasing mitochondrial ROS generated via reverse electron transport, J. Pineal Res. 73 (2022), https://doi.org/10.1111/JPI.12824.

[5] L. Martinez-Ruiz, J. Florido, C. Rodriguez-Santana, A. López-Rodríguez, A. Guerra-Librero, B.I. Fernández-Gil, P. García-Tárraga, J.M. Garcia-Verdugo, F. Oppel, H. Sudhoff, D. Sánchez-Porras, A. Ten-Steve, J. Fernández-Martínez, P. González-García, I. Rusanova, D. Acuña-Castroviejo, V.S. Carriel, G. Escames, Intratumoral injection of melatonin enhances tumor regression in cell line-derived and patient-derived xenografts of head and neck cancer by increasing mitochondrial oxidative stress, Biomed. Pharmacother. 167 (2023) 115518, https://doi.org/10.1016/J.BIOPHA.2023.115518.

[6] F.-G. Bi, G.-L. A, S. Yq, F. J, M.-R. L, G.-L. S, A. C, R.-S. C, A.-C. D, Q.-H. A, F.-M. J, A.M. Ae, L. Lc, R.F. Jm, E. G, Melatonin enhances cisplatin and radiation cytotoxicity in head and neck squamous cell carcinoma by stimulating mitochondrial ROS generation, apoptosis, and autophagy, Oxid. Med. Cell. Longev. 2019 (2019), https://doi.org/10.1155/2019/7187128.

[7] C. Rodríguez-Santana, A. López-Rodríguez, L. Martinez-Ruiz, J. Florido, O. Cela, N. Capitanio, Y. Ramírez-Casas, D. Acuña-Castroviejo, G. Escames, The relationship between clock genes, Sirtuin 1, and mitochondrial activity in head and neck squamous cell cancer: effects of melatonin treatment, Int. J. Mol. Sci. 24 (2023) 15030, https://doi.org/10.3390/IJMS241915030/S1.

[8] E. Jumaniyazova, A. Lokhonina, D. Dzhalilova, A. Kosyreva, T. Fatkhudinov, Role of microenvironmental components in head and neck squamous cell carcinoma, J. Personalized Med. 13 (2023) 1616, https://doi.org/10.3390/JPM13111616. Page 1616 **2023**, 13.

[9] M. Najafi, K. Mortezaee, J. Majidpoor, Cancer stem cell (CSC) resistance drivers, Life Sci. 234 (2019), https://doi.org/10.1016/j.lfs.2019.116781.

[10] X. Dai, C. Ma, Q. Lan, T. Xu, 3D bioprinted glioma stem cells for brain tumor model and applications of drug susceptibility, Biofabrication 8 (2016) 45005, https://doi.org/10.1088/1758-5090/8/4/045005.

[11] J. Koch, D. Mönch, A. Maaß, C. Gromoll, T. Hehr, T. Leibold, H.J. Schlitt, M. H. Dahlke, P. Renner, Three dimensional cultivation increases chemo- and radioresistance of colorectal cancer cell lines, PLoS One 16 (2021) e0244513, https://doi.org/10.1371/JOURNAL.PONE.0244513.

[12] M. Tamayo-Angorrilla, J. López de Andrés, G. Jiménez, J.A. Marchal, The biomimetic extracellular matrix: a therapeutic tool for breast cancer research, Transl. Res. 247 (2022) 117–136, https://doi.org/10.1016/J.TRSL.2021.11.008.

[13] I. Serebriiskii, R. Castelló-Cros, A. Lamb, E.A. Golemis, E. Cukierman, Fibroblast-derived 3D matrix differentially regulates the growth and drug-responsiveness of human cancer cells, Matrix Biol. 27 (2008) 573–585, https://doi.org/10.1016/J.MATBIO.2008.02.008.

[14] G. Jiménez, M. Hackenberg, P. Catalina, H. Boulaiz, C. Griñán-Lisón, M.Á. García, M. Perán, E. López-Ruiz, A. Ramírez, C. Morata-Tarifa, E. Carrasco, M. Aguilera, J. A. Marchal, Mesenchymal stem cell's secretome promotes selective enrichment of cancer stem-like cells with specific cytogenetic profile, Cancer Lett. (2018), https://doi.org/10.1016/j.canlet.2018.04.042.

[15] A. Guerra-Librero, B.I. Fernandez-Gil, J. Florido, L. Martinez-Ruiz, C. Rodríguez-Santana, Y.Q. Shen, J.M. García-Verdugo, A. López-Rodríguez, I. Rusanova, A. Quiñones-Hinojosa, D. Acuña-Castroviejo, J. Marruecos, T. De Haro, G. Escames, Melatonin targets metabolism in head and neck cancer cells by regulating mitochondrial structure and function, Antioxidants 10 (2021) 603, https://doi.org/10.3390/ANTIOX10040603/S1.

[16] M. Chahbouni, G. Escames, C. Venegas, B. Sevilla, J.A. García, L.C. López, A. Muñoz-Hoyos, A. Molina-Carballo, D. Acuna-Castroviejo, Melatonin treatment normalizes plasma pro-inflammatory cytokines and nitrosative/oxidative stress in patients suffering from Duchenne muscular dystrophy, J. Pineal Res. 48 (2010) 282–289, https://doi.org/10.1111/J.1600-079X.2010.00752.X.

[17] L. Thorrez, K. DiSano, J. Shansky, H. Vandenburgh, Engineering of human skeletal muscle with an autologous deposited extracellular matrix, Front. Physiol. 9 (2018) 385279, https://doi.org/10.3389/FPHYS.2018.01076/BIBTEX.

[18] R. Kaukonen, G. Jacquemet, H. Hamidi, J. Ivaska, Cell-derived matrices for studying cell proliferation and directional migration in a complex 3D microenvironment, Nat. Protoc. (12) (2017 1211 2017) 2376–2390, https://doi.org/10.1038/nprot.2017.107.

[19] M.E. Prince, R. Sivanandan, A. Kaczorowski, G.T. Wolf, M.J. Kaplan, P. Dalerba, I. L. Weissman, M.F. Clarke, L.E. Ailles, Identification of a subpopulation of cells with cancer stem cell properties in head and neck squamous cell carcinoma, Proc. Natl. Acad. Sci. U. S. A 104 (2007) 973–978, https://doi.org/10.1073/pnas.0610117104.

[20] K. Vukovic Đerfi, T. Vasiljevic, T. Matijevic Glavan, Recent advances in the targeting of head and neck cancer stem cells, Appl. Sci. 13 (2023), https://doi.org/10.3390/app132413293.

[21] S.R. Martens-de Kemp, A. Brink, M. Stigter-van Walsum, J.M.A. Damen, F. Rustenburg, T. Wu, W.N. Van Wieringen, G.J. Schuurhuis, B.J.M. Braakhuis, M. Slijper, R.H. Brakenhoff, CD98 marks a subpopulation of head and neck squamous cell carcinoma cells with stem cell properties, Stem Cell Res. 10 (2013) 477–488, https://doi.org/10.1016/j.scr.2013.02.004.

[22] C.H. Wong, K.W. Siah, A.W. Lo, Estimation of clinical trial success rates and related parameters, Biostatistics 20 (2019) 273–286, https://doi.org/10.1093/BIOSTATISTICS/KXX069.

[23] A.P. Bonartsev, B. Lei, M.S. Kholina, K.A. Menshikh, D.S. Svyatoslavov, S. I. Samoylova, M.Y. Sinelnikov, V.V. Voinova, K.V. Shaitan, M.P. Kirpichnikov, I. V. Reshetov, Models of head and neck squamous cell carcinoma using bioengineering approaches, Crit. Rev. Oncol. Hematol. 175 (2022) 103724, https://doi.org/10.1016/J.CRITREVONC.2022.103724.

[24] Hoshiba, T. Decellularized extracellular matrix for cancer research. Mater. 2019, Vol. 12, *Page 1311* **2019**, 12, 1311, doi:10.3390/MA12081311.

[25] M. Rafaeva, A.R.D. Jensen, E.R. Horton, K.W. Zornhagen, J.E. Strøbech, L. Fleischhauer, A.E. Mayorca-Guiliani, S.R. Nielsen, D.S. Grønseth, F. Kuś, E. M. Schoof, L. Arnes, M. Koch, H. Clausen-Schaumann, V. Izzi, R. Reuten, J.T. Erler, Fibroblast-derived matrix models desmoplastic properties and forms a prognostic signature in cancer progression, Front. Immunol. 14 (2023) 1154528, https://doi.org/10.3389/FIMMU.2023.1154528/BIBTEX.

[26] M.T. Scherzer, S. Waigel, H. Donninger, V. Arumugam, W. Zacharias, G. Clark, L. J. Siskind, P. Soucy, L. Beverly, Fibroblast-derived extracellular matrices: an alternative cell culture System that increases metastatic cellular properties, PLoS One 10 (2015) e0138065, https://doi.org/10.1371/JOURNAL.PONE.0138065.

[27] W.H. Zhou, W.D. Du, Y.F. Li, M.A. Al-Aroomi, C. Yan, Y. Wang, Z.Y. Zhang, F. Y. Liu, C.F. Sun, The overexpression of fibronectin 1 promotes cancer progression and associated with M2 macrophages polarization in head and neck squamous cell carcinoma patients, Int. J. Gen. Med. 15 (2022) 5027–5042, https://doi.org/10.2147/IJGM.S364708.

[28] S. Gopal, L. Veracini, D. Grall, C. Butori, S. Schaub, S. Audebert, L. Camoin, E. Baudelet, A. Adwanska, S. Beghelli-De La Forest Divonne, S.M. Violette, P. H. Weinreb, S. Rekima, M. Ilie, A. Sudaka, P. Hofman, E. Van Obberghen-Schilling, Fibronectin-guided migration of carcinoma collectives, Nat. Commun. 81 (8) (2017) 1–15, https://doi.org/10.1038/ncomms14105, 2017.

[29] S. Nurmenniemi, M.K. Koivula, P. Nyberg, T. Tervahartiala, T. Sorsa, P.S. Mattila, T. Salo, J. Risteli, Type I and III collagen degradation products in serum predict patient survival in head and neck squamous cell carcinoma, Oral Oncol. 48 (2012) 136–140, https://doi.org/10.1016/J.ORALONCOLOGY.2011.09.002.

[30] C. Zhu, L. Gu, Z. Liu, J. Li, M. Yao, C. Fang, Correlation between vascular endothelial growth factor pathway and immune microenvironment in head and neck squamous cell carcinoma, BMC Cancer 21 (2021) 1–11, https://doi.org/10.1186/S12885-021-08547-4/FIGURES/7.

[31] M.E. Marshall, T.K. Hinz, S.A. Kono, K.R. Singleton, B. Bichon, K.E. Ware, L. Marek, B.A. Frederick, D. Raben, L.E. Heasley, Fibroblast growth factor receptors are components of autocrine signaling networks in head and neck squamous cell carcinoma cells, Clin. Cancer Res. 17 (2011) 5016–5025, https://doi.org/10.1158/1078-0432.CCR-11-0050/84242/AM/FIBROBLAST-GROWTH-FACTOR-RECEPTORS-ARE-COMPONENTS.

[32] S. Ninck, C. Reisser, G. Dyckhoff, B. Helmke, H. Bauer, C. Herold-Mende, Expression profiles of angiogenic growth factors in squamous cell carcinomas of the head and neck, Int. J. Cancer 106 (2003) 34–44, https://doi.org/10.1002/IJC.11188.

[33] G. Miserocchi, C. Cocchi, A. De Vita, C. Liverani, C. Spadazzi, S. Calpona, G. Di Menna, M. Bassi, G. Meccariello, G. De Luca, A. Campobassi, M.M. Tumedei, A. Bongiovanni, V. Fausti, F. Cotelli, T. Ibrahim, L. Mercatali, Three-dimensional collagen-based scaffold model to study the microenvironment and drug-resistance mechanisms of oropharyngeal squamous cell carcinomas, Cancer Biol. Med. 18 (2021) 502–516, https://doi.org/10.20892/J.ISSN.2095-3941.2020.0482.

[34] A.A. Bhat, P. Yousuf, N.A. Wani, A. Rizwan, S.S. Chauhan, M.A. Siddiqi, D. Bedognetti, W. El-Rifai, M.P. Frenneaux, S.K. Batra, M. Haris, M.A. Macha, Tumor microenvironment: an evil nexus promoting aggressive head and neck squamous cell carcinoma and avenue for targeted therapy, Signal Transduct. Targeted Ther. (6) (2020 61 2021) 1–15, https://doi.org/10.1038/s41392-020-00419-w.

[35] D. Dorna, J. Paluszczak, Targeting cancer stem cells as a strategy for reducing chemotherapy resistance in head and neck cancers, J. Cancer Res. Clin. Oncol. 149 (2023) 13417–13435, https://doi.org/10.1007/S00432-023-05136-9, 2023 14914.

[36] A.E. Herzog, K.A. Warner, Z. Zhang, E. Bellile, M.A. Bhagat, R.M. Castilho, G. T. Wolf, P.J. Polverini, A.T. Pearson, J.E. Nör, The IL-6R and Bmi-1 axis controls self-renewal and chemoresistance of head and neck cancer stem cells, Cell Death Dis. 12 (2021 1211 2021) 1–12, https://doi.org/10.1038/s41419-021-04268-5.

[37] X.X. Lv, X.Y. Zheng, J.J. Yu, H.R. Ma, C. Hua, R.T. Gao, EGFR enhances the stemness and progression of oral cancer through inhibiting autophagic degradation of SOX2, Cancer Med. 9 (2020) 1131–1140, https://doi.org/10.1002/CAM4.2772.

[38] J. López de Andrés, C. Griñán-Lisón, G. Jiménez, J.A. Marchal, Cancer stem cell secretome in the tumor microenvironment: a key point for an effective personalized cancer treatment, J. Hematol. Oncol. 13 (2020).

[39] J. Kort-Mascort, M.L. Shen, E. Martin, S. Flores-Torres, L.A. Pardo, P.M. Siegel, S. D. Tran, J. Kinsella, Bioprinted cancer-stromal in-vitro models in a decellularized ECM-based bioink exhibit progressive remodeling and maturation, Biomed. Mater. 18 (2023) 045022, https://doi.org/10.1088/1748-605X/ACD830.

[40] J. Kort-Mascort, G. Bao, O. Elkashty, S. Flores-Torres, J.G. Munguia-Lopez, T. Jiang, A.J. Ehrlicher, L. Mongeau, S.D. Tran, J.M. Kinsella, Decellularized extracellular matrix composite hydrogel bioinks for the development of 3D bioprinted head and neck in vitro tumor models, ACS Biomater. Sci. Eng. 7 (2021) 5288–5300, https://doi.org/10.1021/ACSBIOMATERIALS.1C00812/SUPPL_FILE/AB1C00812_SI_001.PDF.

[41] M. Najafi, K. Mortezaee, J. Majidpoor, Cancer stem cell (CSC) resistance drivers, Life Sci. 234 (2019) 116781, https://doi.org/10.1016/J.LFS.2019.116781.

[42] C.R. Moya-Garcia, H. Okuyama, N. Sadeghi, J. Li, M. Tabrizian, N.Y.K. Li-Jessen, In vitro models for head and neck cancer: current status and future perspective, Front. Oncol. 12 (2022) 960340, https://doi.org/10.3389/FONC.2022.960340/BIBTEX.

[43] J. New, L. Arnold, M. Ananth, S. Alvi, M. Thornton, L. Werner, O. Tawfik, H. Dai, Y. Shnayder, K. Kakarala, T.T. Tsue, D.A. Girod, W.X. Ding, S. Anant, S.M. Thomas, Secretory autophagy in cancer-associated fibroblasts promotes head and neck cancer progression and offers a novel therapeutic target, Cancer Res. 77 (2017) 6679–6691, 10.1158/0008-5472.CAN-17-1077/652996/AM/SECRETORY-AUTOPHAGY-IN-CANCER-ASSOCIATED.

[44] J.H. Choi, B.S. Lee, J.Y. Jang, Y.S. Lee, H.J. Kim, J. Roh, Y.S. Shin, H.G. Woo, C. H. Kim, Single-cell transcriptome profiling of the stepwise progression of head and neck cancer, Nat. Commun. 141 (14) (2023) 1–13, https://doi.org/10.1038/s41467-023-36691-x, 2023.

[45] A.M. Knops, A. South, U. Rodeck, U. Martinez-Outschoorn, L.A. Harshyne, J. Johnson, A.J. Luginbuhl, J.M. Curry, Cancer-associated fibroblast density, prognostic characteristics, and recurrence in head and neck squamous cell carcinoma: a meta-analysis, Front. Oncol. 10 (2020) 565306, https://doi.org/10.3389/FONC.2020.565306/BIBTEX.

[46] H. Zhao, E. Jiang, Z. Shang, 3D Co-culture of Cancer-Associated Fibroblast with Oral Cancer Organoids (2020) 201–208, https://doi.org/10.1177/0022034520956614.

[47] S. Principe, S. Mejia-Guerrero, V. Ignatchenko, A. Sinha, A. Ignatchenko, W. Shi, K. Pereira, S. Su, S.H. Huang, B. O'Sullivan, W. Xu, D.P. Goldstein, I. Weinreb, L. Ailles, F.F. Liu, T. Kislinger, Proteomic analysis of cancer-associated fibroblasts reveals a paracrine role for MFAP5 in human oral tongue squamous cell carcinoma, J. Proteome Res. 17 (2018) 2045–2059, https://doi.org/10.1021/ACS.JPROTEOME.7B00925/SUPPL_FILE/PR7B00925_SI_003.XLSX.

[48] P.N. Le, S.B. Keysar, B. Miller, J.R. Eagles, T.S. Chimed, J. Reisinger, K.E. Gomez, C. Nieto, B.C. Jackson, H.L. Somerset, J.J. Morton, X.J. Wang, A. Jimeno, Wnt signaling dynamics in head and neck squamous cell cancer tumor-stroma interactions, Mol. Carcinog. 58 (2019) 398–410, https://doi.org/10.1002/MC.22937.

[49] S. Álvarez-Teijeiro, C. García-Inclán, M.Á. Villaronga, P. Casado, F. Hermida-Prado, R. Granda-Díaz, J.P. Rodrigo, F. Calvo, N. Del-Río-ibisate, A. Gandarillas, F. Morís, M. Hermsen, P. Cutillas, J.M. García-Pedrero, Factors secreted by cancer-associated fibroblasts that sustain cancer stem properties in head and neck squamous carcinoma cells as potential therapeutic targets, Cancers 10 (2018), https://doi.org/10.3390/CANCERS10090334. Page 334 **2018**, 10, 334.

[50] B. Peltanova, M. Liskova, J. Gumulec, M. Raudenska, H.H. Polanska, T. Vaculovic, D. Kalfert, M. Grega, J. Plzak, J. Betka, M. Masarik, Sensitivity to cisplatin in head and neck cancer cells is significantly affected by patient-derived cancer-associated fibroblasts, Int. J. Mol. Sci. 22 (2021), https://doi.org/10.3390/IJMS22041912. Page 1912 2021, 22, 1912.

[51] A.C. Johansson, A. Ansell, F. Jerhammar, M.B. Lindh, R. Grénman, E. Munck-Wikland, A. Östman, K. Roberg, Cancer-associated fibroblasts induce matrix metalloproteinase-mediated cetuximab resistance in head and neck squamous cell carcinoma cells, Mol. Cancer Res. 10 (2012) 1158–1168, https://doi.org/10.1158/1541-7786.MCR-12-0030/79979/AM/CANCER-ASSOCIATED-FIBROBLASTS-INDUCE-MATRIX.

[52] K.M. Yegodayev, O. Novoplansky, A. Golden, M. Prasad, L. Levin, S. Jagadeeshan, J. Zorea, O. Dimitstein, B.Z. Joshua, L. Cohen, E. Khrameeva, M. Elkabets, TGF-Beta-Activated cancer-associated fibroblasts limit cetuximab efficacy in preclinical models of head and neck cancer, Cancers 12 (2020), https://doi.org/10.3390/CANCERS12020339. *Page 339* 2020, 12, 339.

[53] K.M. Hakkinen, J.S. Harunaga, A.D. Doyle, K.M. Yamada, Direct Comparisons of the Morphology, Migration, Cell Adhesions, and Actin Cytoskeleton of Fibroblasts in Four Different Three-Dimensional Extracellular Matrices (2010.0273), https://doi.org/10.1089/TEN.TEA.

[54] L. Wang, C. Wang, W.S. Choi, Use of melatonin in cancer treatment: where are we? Int. J. Mol. Sci. 23 (2022) https://doi.org/10.3390/IJMS23073779. Page 3779 2022, 23, 3779.

[55] Y. Wang, B. Tao, J. Li, X. Mao, W. He, Q. Chen, Melatonin inhibits the progression of oral squamous cell carcinoma via inducing miR-25-5p expression by directly targeting NEDD9, Front. Oncol. 10 (2020) 543591, https://doi.org/10.3389/FONC.2020.543591/BIBTEX.

[56] S. Dholariya, R.D. Singh, K.A. Patel, Melatonin: emerging player in the management of oral cancer, Crit. Rev. Oncog. 28 (2) (2023) 77–92, https://doi.org/10.1615/CritRevOncog.2023048934.

[57] M. Akbarzadeh, A.A. Movassaghpour, H. Ghanbari, M. Kheirandish, N. Fathi Maroufi, R. Rahbarghazi, M. Nouri, N. Samadi, The potential therapeutic effect of melatonin on human ovarian cancer by inhibition of invasion and migration of cancer stem cells, Sci. Rep. (7) (2017 71 2017) 1–11, https://doi.org/10.1038/s41598-017-16940-y.

[58] P.P. Phiboonchaiyanan, P. Puthongking, V. Chawjarean, S. Harikarnpakdee, M. Sukprasansap, P. Chanvorachote, A. Priprem, P. Govitrapong, Melatonin and its derivative disrupt cancer stem-like phenotypes of lung cancer cells via AKT downregulation, Clin. Exp. Pharmacol. Physiol. 48 (2021) 1712–1723, https://doi.org/10.1111/1440-1681.13572.

[59] N.F. Maroufi, V. Vahedian, S. Hemati, M.R. Rashidi, M. Akbarzadeh, M. Zahedi, F. Pouremamali, A. Isazadeh, S. Taefehshokr, S. Hajazimian, N. Seraji, M. Nouri, Targeting cancer stem cells by melatonin: effective therapy for cancer treatment, Pathol. Res. Pract. 216 (2020).

[60] X. Luo, J. Wang, Y. Chen, X. Zhou, Z. Shao, K. Liu, Z. Shang, Melatonin inhibits the stemness of head and neck squamous cell carcinoma by modulating HA synthesis via the FOSL1/HAS3 axis, J. Pineal Res. 76 (2024) 1–15, https://doi.org/10.1111/jpi.12940.

[61] K. Tuomainen, A. Al-Samadi, S. Potdar, L. Turunen, M. Turunen, P.R. Karhemo, P. Bergman, M. Risteli, P. Åström, R. Tiikkaja, R. Grenman, K. Wennerberg, O. Monni, T. Salo, Human tumor–derived matrix improves the predictability of head and neck cancer drug testing, Cancers 12 (2020), https://doi.org/10.3390/CANCERS12010092.

[62] B.I. Fernandez-Gil, A. Guerra-Librero, Y.Q. Shen, J. Florido, L. Martínez-Ruiz, S. García-López, C. Adan, C. Rodríguez-Santana, D. Acuña-Castroviejo, A. Quiñones-Hinojosa, J. Fernández-Martínez, A.E. Abdel Moneim, L.C. López, J. M. Rodríguez Ferrer, G. Escames, Melatonin enhances cisplatin and radiation cytotoxicity in head and neck squamous cell carcinoma by stimulating mitochondrial ROS generation, apoptosis, and autophagy, Oxid. Med. Cell. Longev. 2019 (2019), https://doi.org/10.1155/2019/7187128.

[63] Y.Q. Shen, A. Guerra-Librero, B.I. Fernandez-Gil, J. Florido, S. García-López, L. Martinez-Ruiz, M. Mendivil-Perez, V. Soto-Mercado, D. Acuña-Castroviejo, H. Ortega-Arellano, V. Carriel, M.E. Diaz-Casado, R.J. Reiter, I. Rusanova, A. Nieto, L.C. López, G. Escames, Combination of melatonin and rapamycin for head and neck cancer therapy: suppression of AKT/mTOR pathway activation, and activation of mitophagy and apoptosis via mitochondrial function regulation, J. Pineal Res. 64 (2018) e12461, https://doi.org/10.1111/JPI.12461.

[64] A. Kocyigit, E.M. Guler, E. Karatas, H. Caglar, H. Bulut, Dose-dependent proliferative and cytotoxic effects of melatonin on human epidermoid carcinoma and normal skin fibroblast cells, Mutat. Res. Toxicol. Environ. Mutagen. 829–830 (2018) 50–60, https://doi.org/10.1016/J.MRGENTOX.2018.04.002.

[65] L. Sagrillo-Fagundes, J. Bienvenue-Pariseault, C. Vaillancourt, Melatonin: the smart molecule that differentially modulates autophagy in tumor and normal placental cells, PLoS One 14 (2019) e0202458, https://doi.org/10.1371/JOURNAL.PONE.0202458.

[66] Z. Ma, L. Xu, D. Liu, X. Zhang, S. Di, W. Li, J. Zhang, R.J. Reiter, J. Han, X. Li, X. Yan, Utilizing melatonin to alleviate side effects of chemotherapy: a potentially good partner for treating cancer with ageing, Oxid. Med. Cell. Longev. 2020 (2020), https://doi.org/10.1155/2020/6841581.

[67] A. Balci-Ozyurt, A. Yirün, D.A. Cakır, N.D. Zeybek, D. Oral, S. Sabuncuoğlu, P. Erkekoğlu, Evaluation of possible cytotoxic, genotoxic and epigenotoxic effects of titanium dioxide nanoparticles and possible protective effect of melatonin, Toxicol. Mech. Methods 34 (2024) 109–121, https://doi.org/10.1080/15376516.2023.2259980.

[68] K. Singh, M. Bhori, Y.A. Kasu, G. Bhat, T. Marar, Antioxidants as precision weapons in war against cancer chemotherapy induced toxicity – exploring the armoury of obscurity, Saudi Pharmaceut. J. 26 (2018) 177–190, https://doi.org/10.1016/J.JSPS.2017.12.013.

[69] A. Affolter, A. Lammert, J. Kern, C. Scherl, N. Rotter, Precision medicine gains momentum: novel 3D models and stem cell-based approaches in head and neck cancer, Front. Cell Dev. Biol. 9 (2021) 666515, https://doi.org/10.3389/FCELL.2021.666515/BIBTEX.